



THE FORMATION OF CORES OF GIANT PLANETS AT CONVERGENCE ZONES OF PLANETARY MIGRATION

SIN-ITI SIRONO AND MASAHUMI KATAYAMA

Earth and Planetary Sciences, Nagoya University, Tikusa-ku, Furo-cho, Nagoya 464-8601 Japan
 Received 2014 March 24; revised 2016 May 25; accepted 2016 June 27; published 2016 October 11

ABSTRACT

The formation of solid cores in giant planets of mass $\sim 10 M_{\oplus}$ is numerically simulated following the scenario of Sándor et al. In this scenario, there are two convergence zones, corresponding to the outer and inner edges of the dead zone, where the torque exerted on planetary embryos by the gas nebula is zero. At the outer edge of the dead zone, anticyclonic vortices accumulate infalling dust aggregates, and planetary embryos are continuously formed in this scenario. We performed N -body simulations and show that massive objects of $\simeq 10 M_{\oplus}$ are formed in ~ 2.5 Myr, starting from the embryos. The largest object is formed at the inner convergence zone, although planetary embryos are placed at the outer convergence zone. This is due to the scattering of embryos from the outer to the inner convergence zone, and the shorter damping timescale of eccentricity at the inner convergence zone compared to the outer one. We varied the migration timescale due to the torque from gas by changing the gas surface density around the convergence zones. We found that there is a critical migration timescale below which $10 M_{\oplus}$ -sized objects are formed. Furthermore, we conducted simulations in which the gas surface density evolves according to viscous accretion. The largest object is also formed at the inner convergence zone irrespective of the strength of turbulence. Throughout the simulations, the location of the largest mass is the inner convergence zone. We confirmed that the formation timescale of a core of a Jovian planet can be explained in this scenario.

Key words: methods: numerical – planet–disk interactions – planets and satellites: formation – protoplanetary disks

1. INTRODUCTION

Planetary formation is full of mysteries. There are many unsolved problems in the key evolutionary steps of the evolution of a planetary system. Among them, planetesimal formation and gas giant formation are the most important ones.

There are two major obstacles to planetesimal formation: inward migration and breakup of dust aggregates. Dust aggregates are formed in a protoplanetary nebula through the coagulation of sub-micron-sized dust grains. The mass fraction of dust grains in a protoplanetary nebula is roughly 1%. The other component is gas primarily composed of hydrogen and helium. Dust grains have relative velocities induced by Brownian motion and the turbulence of nebula gas. Collisions between dust grains lead to the formation of dust aggregates, which experience further growth through successive collisions.

Radial migration of an aggregate is induced by the difference in the rotational velocities of a nebula gas and an aggregate. The maximum migration velocity is $\sim 50 \text{ m s}^{-1}$ when the size of an aggregate is $\sim 1 \text{ m}$. At this migration velocity, an aggregate travels a distance of 1 au within ~ 100 years (Weidenschilling 1977). If this is the case, the solid component of a protoplanetary nebula quickly disappears.

Many models have been proposed to halt the inward migration and accumulate aggregates at some location in a protoplanetary nebula. Kretke & Lin (2007) studied the migration velocity change at the snowline. A pressure bump in the nebula gas is formed by the viscosity change at the snowline, and dust aggregates accumulate around the pressure bump. Lyra et al. (2009) simulated anticyclonic vortices formed around the edge of the dead zone, where the degree of turbulence changes greatly. A vortex efficiently traps the migrating aggregate. Sirono (2011) showed that the breakup of icy aggregates induced by sintering leads to an accumulation of the icy dust aggregates. Kato et al. (2010) conducted MHD

simulations with an electrical conductivity gap, which induces a pressure bump and an accumulation of dust aggregates.

Similarly, giant planet formation suffers from two problems: the formation timescale and inward migration. Observationally, the lifetime of nebula gas is on the order of $1 \sim 10$ Myr (Haisch et al. 2001). In the core accretion scenario, a core of a gas giant should grow to the critical core mass ($\sim 10 M_{\oplus}$) through the accretion of the nebula gas before the dispersal. However, the quick formation mechanism of a core is uncertain. Many attempts have been made to shorten the formation timescale of a solid core (a brief review is given in Levison et al. 2010). However, no consensus has yet been reached.

Gravitational interaction between a planetary embryo and nebula gas causes Type I migration (Tanaka et al. 2002). The timescale of Type I migration is ~ 1 Myr for a $1 M_{\oplus}$ object, which is sufficiently short compared to the lifetime of nebula gas. This “inward migration problem” of planets has been the most troublesome problem in planetary formation. However, it has been shown that the direction of the planetary migration can change according to the density and temperature distributions of nebula gas (Paardekooper & Mellema 2006). A planet can migrate outward if these conditions are met. Hasegawa & Pudritz (2011) showed the existence of many convergence zones where the torque on a planet becomes zero and a planet orbits stably. The convergence zones are formed by different mechanisms, including the sublimation of ice or silicates, a change in heating source, and a transition of turbulence.

We have discussed the existing problems in planetesimal and gas giant formation. Because these two formation events occur successively in a protoplanetary nebula, they might be solved by a single key mechanism. Such an attempt was performed by Sándor et al. (2011). Their work is based on Lyra et al. (2009), who showed that inward-migrating dust aggregates are trapped by an anticyclonic vortex. A vortex is formed at the edge of the dead zone in which the turbulent viscosity drops because of the

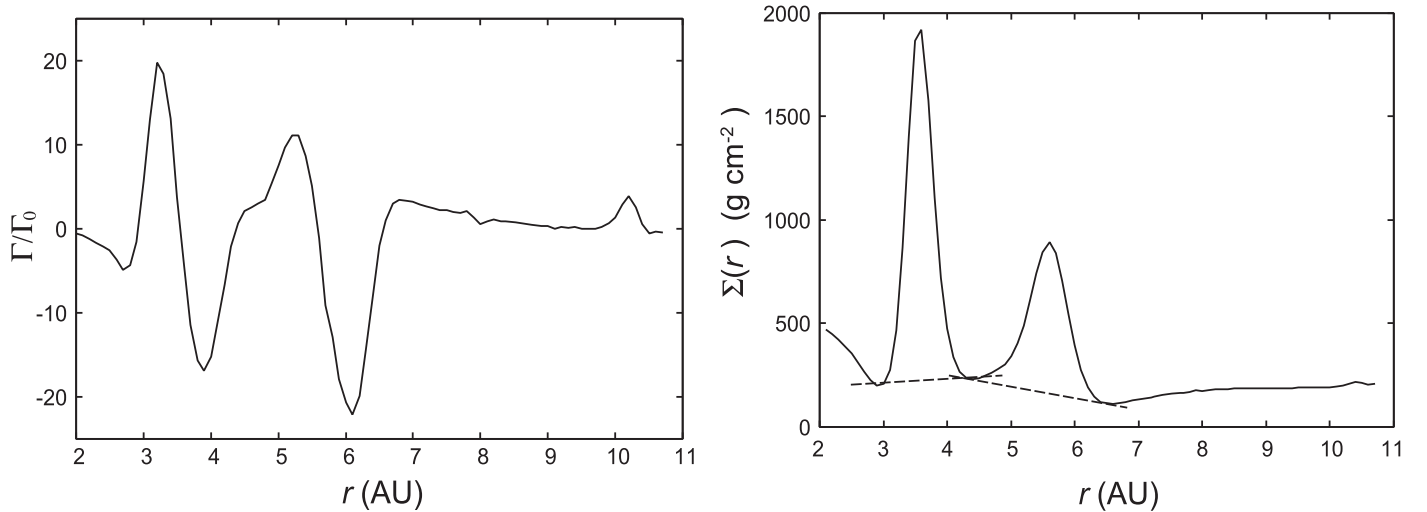


Figure 1. Normalized torque Γ/Γ_0 (left) and surface density $\Sigma(r)$ (right) distributions in this study, reproduced from Sándor et al. (2011). There are two convergence zones located at 3.6 and 5.6 au where Γ/Γ_0 changes its sign from positive to negative as r increases. The two dashed lines in the right panel are the baselines to modify the heights of the peaks (see Section 3.2).

low electrical conductivity of nebula gas. The mass of the trapped dust aggregates reaches $\sim 1/3 M_\oplus$ in 5000 years. We can expect that a planetary embryo of $\sim 1/3 M_\oplus$ is formed every 5000 years if the vortices are continuously formed at the edge of the dead zone. Moreover, Lyra et al. (2009) found two pressure bumps at both (inner and outer) edges of the dead zone. These bumps become the convergence zones of planets. Based on these findings, Sándor et al. (2011) conducted N -body simulations and showed that a solid core of mass $10 M_\oplus$ is formed in 0.4 Myr, which is sufficiently shorter than the lifetime of nebula gas.

Although their calculation is simple, their scenario is attractive because the two major unsolved problems, planetesimal and gas giant formation, can be solved simultaneously. However, as we will see later, they adopted inappropriate formulas for the damping timescales of eccentricity and inclination of a protoplanet induced by nebula gas. In this paper, we conduct N -body simulations using the same scenario as Sándor et al. (2011) and check the scenario. In particular, we conduct a number of simulations and determine the distribution of the formation timescale of a solid core of mass $10 M_\oplus$.

There are two convergence zones corresponding to the outer and inner edges of the dead zone. Although the gas surface density distribution is fixed in Sándor et al. (2011), it would evolve. As a first step, we change the heights of the two peaks of the gas density distribution. We determine the dependence of the largest mass and its formation time on the heights. Furthermore, a one-dimensional (1D) model of the viscous evolution of the gas surface density is adopted to simulate the time evolution. Distributions of the largest mass and formation time are obtained. Through these simulations, we try to constrain parameters relevant to this scenario, including the heights of the two peaks and the strength of viscosity.

In the next section, basic equations are presented, and we discuss how they differ from those in Sándor et al. (2011). In Section 3, the results of the numerical simulations are shown. The relevance of the numerical results in the scenario of Sándor et al. (2011) is discussed in Section 4. Conclusions are given in the final section.

2. BASIC EQUATIONS

The acceleration of the i th object at position \mathbf{r}_i is determined from the gravitational force exerted by other bodies with masses m_j and the contributions from the nebula gas,

$$\ddot{\mathbf{r}}_i = -\sum_j \frac{Gm_j\mathbf{r}_{ij}}{r_{ij}^3} - \frac{\dot{\mathbf{r}}_i}{2\tau_{\text{migr}}} - 2\frac{(\mathbf{r}_i \cdot \dot{\mathbf{r}}_i)\mathbf{r}_i}{r_i^2\tau_{\text{ecc}}} - \frac{(\dot{\mathbf{r}}_i \cdot \mathbf{k})\mathbf{k}}{\tau_{\text{inc}}}, \quad (1)$$

where \mathbf{r}_{ij} is a position vector from i to j , \mathbf{k} is the unit vector in the z -direction, and G is the gravitational constant. In Equation (1), τ_{migr} , τ_{ecc} , and τ_{inc} are the damping timescales for radial migration, eccentricity, and inclination, respectively. The radial migration timescale (positive: outward migration) of an object of mass m is given by

$$\tau_{\text{migr}} = \frac{h^2 M_*^{3/2}}{-2m \frac{\Gamma}{\Gamma_0} \Sigma(r) r^2 \sqrt{rG}}, \quad (2)$$

where r is the distance from the central star, M_* is the mass of the central star, h is the gas scale height, Σ is gas surface density, and Γ/Γ_0 is the normalized torque on a protoplanet ($\Gamma_0 = (m/hM_*)^2 \Sigma(r) r^4 \Omega(r)^2$, where Ω is the Keplerian frequency). As in Sándor et al. (2011), we assume locally isothermal disks and Γ/Γ_0 is given by

$$\frac{\Gamma}{\Gamma_0} = -0.85 - \alpha - 0.9\beta, \quad (3)$$

where α and β are the gradients of surface density $\Sigma(r)$ and temperature $T(r)$ given by

$$\alpha = -\frac{d \log \Sigma}{d \log r}, \quad \beta = -\frac{d \log T}{d \log r}. \quad (4)$$

We adopt a constant $\beta = 1$, except for simulations with evolving gas surface density (see Section 3.3). For Γ/Γ_0 and $\Sigma(r)$, the distributions in Sándor et al. (2011) are used (see Figure 1). A constant timescale of $\tau_{\text{migr}} = 1$ Myr is adopted inside and outside of the region shown in Figure 1. Basically, simulations are performed using the surface density distribution $\Sigma(r)$ shown in Figure 1. This is the standard case. In addition to

the standard case, we change the heights of the two peaks in $\Sigma(r)$ and check the dependence on the heights. To modify the peak heights, the difference between the curve forming a peak and the baseline (Figure 1 right) is multiplied by a factor C (see Section 3.2). Moreover, the gas surface density distribution is evolved according to the viscous accretion of a disk (see Section 3.3).

The timescales for eccentricity (e) damping τ_{ecc} and inclination (i) damping τ_{inc} are respectively given by (Cresswell & Nelson 2008) as

$$\begin{aligned}\tau_{\text{ecc}} &= \frac{\tau_{\text{damp}}}{0.780} \left[1 - 0.14 \left(\frac{e}{h} \right)^2 + 0.06 \left(\frac{e}{h} \right)^3 \right. \\ &\quad \left. + 0.18 \left(\frac{e}{h} \right) \left(\frac{i}{h} \right)^2 \right], \\ \tau_{\text{inc}} &= \frac{\tau_{\text{damp}}}{0.544} \left[1 - 0.30 \left(\frac{i}{h} \right)^2 + 0.24 \left(\frac{i}{h} \right)^3 \right. \\ &\quad \left. + 0.14 \left(\frac{i}{h} \right) \left(\frac{e}{h} \right)^2 \right],\end{aligned}\quad (5)$$

where $\tau_{\text{damp}} = M_*^2 h^4 / m \Sigma a^2 \Omega \simeq h^4 M_*^{3/2} / m \Sigma \sqrt{rG} \simeq h^2 \tau_{\text{migr}}$ (a : semimajor axis of the planet). An impulse approximation (Armitage 2010) shows that the one-side torque (gas torque exerted from outside or inside of a planetary orbit) is proportional to h^{-3} . Because the inclination and eccentricity damping timescales should be proportional to the gas density (inversely proportional to h), another h^{-1} factor is multiplied. As a result, τ_{damp} is proportional to h^4 . On the other hand, the migration timescale is proportional to the difference between the outside and inside torque. This difference is proportional to the thickness of the gas disk (proportional to h), and the migration timescale dependence becomes h^{-2} .

The formulas are different from those of Sándor et al. (2011), where $\tau_{\text{ecc}}, \tau_{\text{inc}} \sim h^4 \tau_{\text{migr}}$ are adopted. Therefore, an additional factor of h^2 is multiplied to the formula in Sándor et al. (2011) to obtain Equation (5). This multiplication shortens the timescales by a factor of ~ 100 . Eccentricity and inclination damping in this study are slower than those in Sándor et al. (2011). It can be expected that the application of Equation (5) leads to more excited, chaotic motion of planetary embryos.

We have fixed the gas surface density distributions above. To simulate more realistic cases, the distribution is evolved according to a simple one-dimensional model (Armitage 2010) given by

$$\frac{\partial \Sigma}{\partial t} = \frac{3}{r} \frac{\partial}{\partial r} \left[r^{1/2} \frac{\partial}{\partial r} (\nu \Sigma r^{1/2}) \right], \quad (6)$$

where ν is the kinematic viscosity. As shown by Regály et al. (2013), the shift of the center of mass was observed in a two-dimensional (2D) system, which affects the capturing of an object. This feature cannot be simulated in a 1D system. However, it is difficult to conduct a long-term simulation in a 2D system that covers the growth and decline of a peak in Σ . The growth and decline of a peak in Σ distribution is a key mechanism for trapping an object at a convergence zone, as shown later.

In this model, the kinematic viscosity ν is written as $\nu = \alpha c_s^2 \Omega$ (α : non-dimensional viscosity parameter, c_s : sound

speed). At the inner and outer edges, the viscous α parameter changes because turbulence is weak inside the dead zone. In this study, it is assumed that $\alpha = \alpha_0$ outside the dead zone, and reduced to $0.01\alpha_0$ inside the dead zone as

$$\frac{\alpha(r)}{\alpha_0} = 1 - \frac{0.99}{2} \left[\tanh \left(\frac{r - r_1}{\Delta_1} \right) - \tanh \left(\frac{r - r_2}{\Delta_2} \right) \right], \quad (7)$$

where r_1 and r_2 are the locations of inner and outer edges of a dead zone, and Δ_1 and Δ_2 are the thicknesses of the inner and outer edges, respectively. Basically, we set both thicknesses to the gas scale heights h at both edges. In the following, we denote the ratio between the thicknesses to the gas scale height by Δ/h . The standard condition is $\Delta/h = 1$. We have also tested $\Delta/h = 10$ cases, and checked the effects (see Section 3.3). It should be noted that in a 2D model, trapping of $10 M_{\oplus}$ is only observed in small thickness cases (Regály et al. 2013). Three sets of r_1 and r_2 are tested: ($r_1 = 0.1$ au, $r_2 = 5.6$ au), ($r_1 = 0.1$ au, $r_2 = 12$ au), and ($r_1 = 1$ au, $r_2 = 5.6$ au). The inner edge at $r_1 = 0.1$ au is originally derived in Gammie (1996). The outer edge at $r_2 = 12$ au is adopted from Regály et al. (2013). For comparison, the location of the outer edge $r_2 = 5.6$ au from Sándor et al. (2011) and $r_1 = 1$ au are tested. As done in the standard case, planetary embryos of $1/3 M_{\oplus}$ are placed at the outer edge of the dead zone.

The gas temperature distribution $T(r)$ is given by

$$T(r) = T_0 \left(\frac{r}{1 \text{ au}} \right)^{-1/2}, \quad (8)$$

where $T_0 = 280$ K. In this case, the parameter β in Equation (4) is 0.5, and this value is used in calculations of torques.

The left panel of Figure 2 shows the evolution of gas surface density according to Equation (6) for $\alpha_0 = 10^{-3}$. At the beginning, two peaks of Σ are formed at the inner and outer edges of the dead zone. Correspondingly, two convergence zones are formed at both edges. Then the peaks of Σ expand into the dead zone. Outside the dead zone, Σ decreases due to accretion. After $t = 10^6$ years, two peaks of Σ disappear and a large bump remains at the dead zone. It should be noted that only the inner convergence zone survives and the outer one disappears (Figure 2(b)). At the outer edge, Σ steeply decreases as r increases and only inward migration is possible.

The time evolution of Σ is inversely proportional to α_0 . For example, the curve labeled 10^6 years corresponds to 10^7 years for $\alpha_0 = 10^{-4}$. Therefore, the lifetime of the outer convergence zone is long for small α_0 .

The settings of N -body simulations are set to be as similar to those in Sándor et al. (2011) as possible. Initially, 10 embryos of $1/3 M_{\oplus}$ are placed at the outer convergence zone (5.6 au or 12 au) with random azimuthal positions. An embryo is newly formed at the same heliocentric distance, with a Poisson distribution of the mean interval of 5000 years. If the distance between two objects becomes less than the sum of the two radii, the two objects merge without fragmentation. The formation of the new embryos lasts for 0.5 Myr, and the average number of newly formed embryos is 100. The simulation is terminated at 10 Myr, which is longer than the simulation employed by Sándor et al. (2011), in which simulation results are shown up to 0.5 Myr. We performed 100 simulations with different random timings of embryo

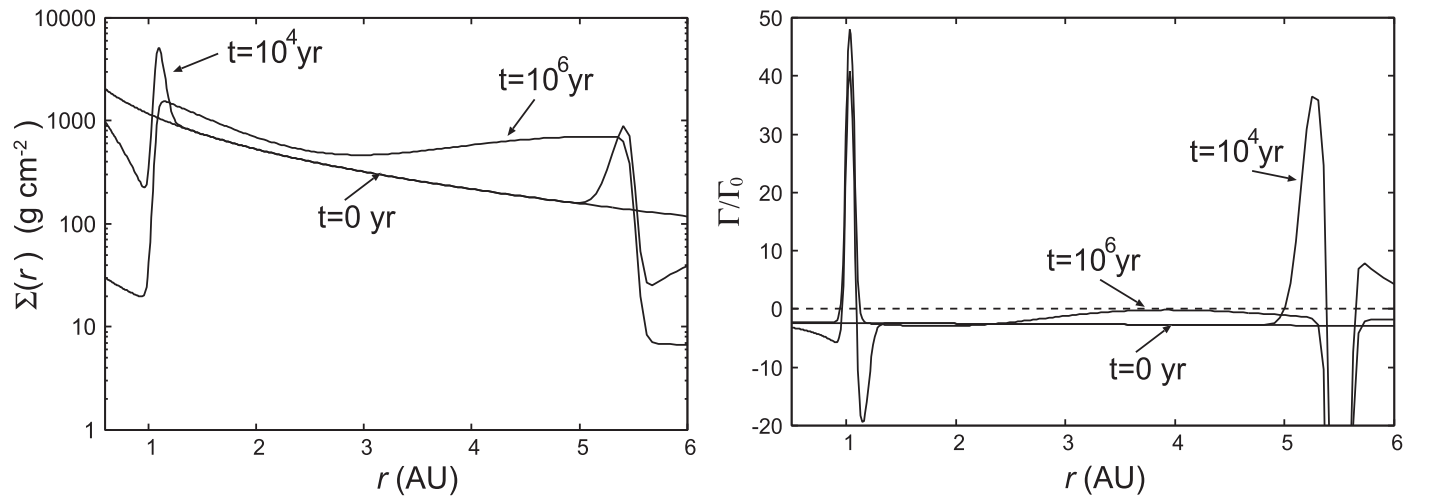


Figure 2. Evolution of the gas surface density (left) and torque (right) for $\alpha_0 = 10^{-3}$. Distributions at three periods ($t = 0, 10^4$, and 10^6 years) are shown. After 10^6 years, the convergence zone at the outer edge disappears.

formation, and obtained the distributions of formation time and mass of solid cores. For simulations with evolving surface density, 50 simulations are conducted. Viscous parameter α_0 is varied between 10^{-2} and 10^{-5} . If $\alpha_0 = 10^{-2}$, the outer convergence zone disappears within 0.1 Myr. Because the embryos are formed by infalling aggregates at the outer edge in this scenario, the formation duration of new embryos for 0.5 Myr at the outer edge is not reasonable in this case. For $\alpha_0 = 10^{-2}$, we carried out another case in which the embryos are formed at $r_1 = 1$ au and other parameters are given by $r_2 = 5.6$ au, and $\Delta/h = 1$.

Simulations are performed using the Mercury-6 code (Chambers 1999) with a modification for the external force (Equation (1)) from the nebula gas. The transition distance between the Symplectic and Bulirsch–Stoer solver is 5 Hill radius. A fixed timestep of 8 d is adopted.

3. NUMERICAL RESULTS

3.1. Standard Case

First we attempted to reproduce the results of Sándor et al. (2011) by multiplying a factor of h^2 artificially to Equation (5). The left panels of Figure 3 shows the evolution of the semimajor axis, mass, and eccentricity of the top 10 massive objects. This result is quantitatively similar to that obtained in Sándor et al. (2011). When an embryo is newly formed, a large perturbation is induced. These perturbations lead to collisions between objects, which can be seen as growth of the objects (middle left panel). The width of the system gradually increases as the largest object grows. The mass of the largest object exceeds $10 M_\oplus$ at 0.25 Myr. The largest object is located around the outer convergence zone at 5.6 au, and it is surrounded by lighter objects at mean motion resonances of the largest object. The two objects in the outer part of the system (8.5 and 9.4 au at 1 Myr) gradually drift outward because of the positive torques there (see Figure 1). Light objects are pushed inward and stably reside at around the inner convergence zone (3.6 au). During the entire evolution, the eccentricity of the largest object is kept small between 10^{-4} and 10^{-3} . The eccentricity of light objects is on the order of 10^{-2} .

The evolution drastically changes when we apply Equation (5) as the damping timescales of eccentricity and

inclination. The orbital evolution is shown in the top right panel of Figure 3. The evolution is more chaotic, especially in the first 2 Myr before the formation of a $10 M_\oplus$ object. During this period, every object performs complex motion, perturbing each other. This is expected from the difference of a factor of h^2 . It should be noted that the x -axis of this figure is 10 times longer than that of the left panel. This corresponds to the evolutionary timescale of this system, which is longer than those of the left panels. Up to 1 Myr, there are two objects of $2 M_\oplus$ located at the outer convergence zone. Their masses are nearly identical during this period. After 2 Myr, the mass of the largest object at the inner convergence zone dominates over that of the outer one and reaches $10 M_\oplus$. It should be noted that the planetary embryos are formed only at the outer convergence zone. Nevertheless, the largest object is formed at the inner convergence zone. This fact suggests that there is efficient transport of embryos from the outer to the inner convergence zone by long-lasting perturbed motions.

After 2 Myr, the chaotic motions of the objects are not observed, and the system enters a stable evolution phase. The mass of the largest object exceeds $10 M_\oplus$ at 2.2 Myr. At this time, the mass of the second largest object is $3.0 M_\oplus$. A light object gradually move outward, as in the left panel, except with irregular motions because of the slow damping of eccentricity and inclination. On the other hand, light objects in the inner zone drift inward, keeping their order. The inward drift comes from the assumption of the constant migration timescale inside 2 au. In the left panel, no inward drift is observed because no object passes 2 au. This difference comes from the fact that a massive object is formed at the inner convergence zone and expels the lighter ones inward in the right panel.

The eccentricities of the two large objects are kept at $\sim 10^{-1}$. Those for the two light objects in the outer region are between 10^{-2} and 10^{-1} . For the inner objects inside 2 au, eccentricity is low, between 10^{-4} and 10^{-3} . This reflects the fact that their eccentricities are damped in a 1 Myr timescale, according to the assumption.

The increase in the mass of the two largest objects stops at around 4 Myr. The remaining embryos are scattered by the two large objects. Combining this scattering with the torque distribution, which is negative inside 2.7 au and positive outside 6.7 au, the regions inside and outside the two

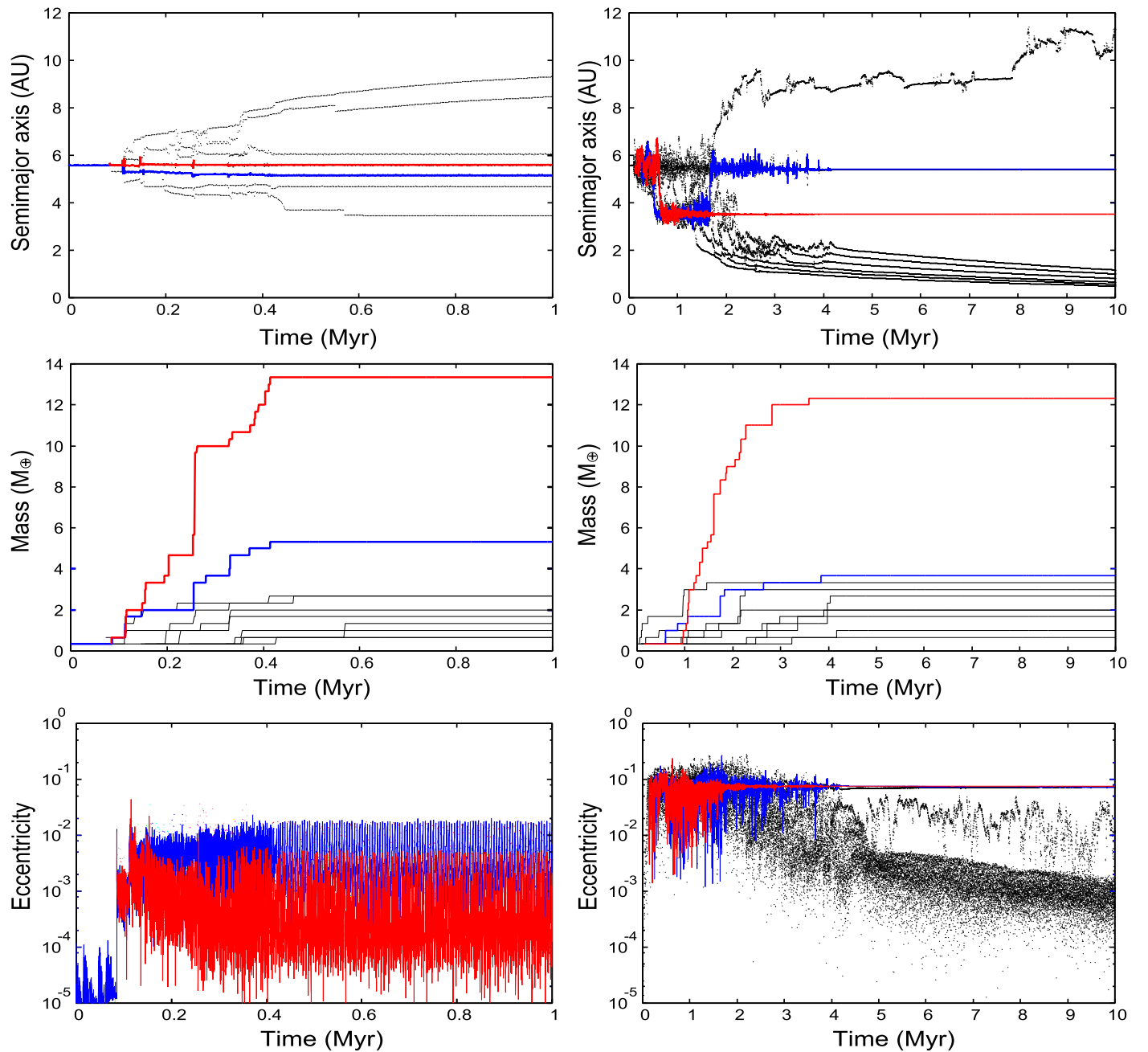


Figure 3. Evolution of the top 10 massive objects' semimajor axes (top), masses (middle), and eccentricities (bottom). Left panel: damping timescales of eccentricity and inclination are multiplied by h^2 to Equation (5). Right panel: same as the left panel, except the timescales are given by Equation (5). The largest and second largest objects are shown by red and blue curves, respectively. The black curves correspond to the remaining eight objects. Note that the range of the horizontal axes of the left panels is shorter than the range of those of the right panels by a factor of 10.

convergence zones are cleared, and the growth of the largest objects stops.

We performed 100 simulations, each under identical settings except for random timings of the embryo formation. Figure 4 shows the histogram of the formation time of the solid core of $10 M_{\oplus}$. The mass of the largest object exceeds $10 M_{\oplus}$ in 81 simulations. It can be seen that the formation time is concentrated between 2 and 3 Myr. This timescale is comparable to the gas nebula lifetime and longer than the 0.4 Myr reported in Sándor et al. (2011). The difference stems from the long timescale of eccentricity and inclination damping. Excited motions of objects in our simulations decrease the chance of a collision with the large objects located at the two convergence zones.

Figure 5 shows the distribution of the mass of the largest object (left) and the second largest object (right) during a simulation. As shown in Figure 4, the mass of the largest object exceeds $10 M_{\oplus}$ in 81 simulations. However, in the other 19 simulations, the mass only exceeds $6 M_{\oplus}$. Similarly, the mass of the second largest objects exceeds $5 M_{\oplus}$ in 57 simulations (Figure 4 right). These results suggest that at least one gas giant can be formed at the inner convergence zone.

The distribution of the orbital positions of the largest and second largest objects is shown in Figure 6. The largest object is located at the inner convergence zone in 96 simulations out of 100. The second largest object is formed at the outer convergence zone in 72 simulations. This result shows efficient

mass transportation from the outer to the inner convergence zone.

3.2. Peak Height Dependence

So far we have fixed the gas surface density distribution $\Sigma(r)$. However, the distribution can change as a protoplanetary disk evolves. It is possible that the position and height of the two peaks change with time. Apart from the dead zone scenario of this study, there are many simulations including the evolution of gaseous nebulae. In these studies, the location of the convergence zones drifts as the gas and temperature distributions evolve (Hellary & Nelson 2012). The locations of protoplanets are strongly affected by these evolutions.

In the context of this study, there are many variable quantities: gas and temperature distributions, mass, location, and formation rate of planetary embryos. As a first step, we change the heights of the two peaks of the gas surface density distribution, keeping all the other quantities fixed. The gas surface distribution is not time-dependent. Planetary embryos are formed at the outer convergence zone (5.6 au). We examine the dependencies of the protoplanets' masses and locations on the heights of the two peaks. It should be noted that the largest

object is formed at the inner convergence zone in the standard case.

The heights of the two peaks are changed as follows. Two straight baselines (Figure 1 right) connect three minimums in $\Sigma(r)$ located at 3.0, 4.4, and 6.5 au. The difference between the curve composing the peak and the baseline is changed by a factor of $C = 2, 1, 0.5, 0.1,$ and 0.01 . Twenty-one combinations of C for inner and outer peaks are tested. $C = 2$ is taken only for the outer peak because the height of the inner peak is roughly twice that of the outer peak in the original distribution. For each combination, 100 simulation runs are performed.

Modification of the peaks leads to a change to the migration timescale around the peak. There are two maximum timescales associated with one peak, one for inward migration and one for outward migration. This is because there are two maxima for the gradient of gas surface density (Equation (4)) for one peak (see Figure 1). The migration timescale around the peak $\tau_{\text{migr,p}}$ is defined as the average of the absolute value of the two maximum timescales. If the factor C is sufficiently small, only inward migration is possible around a peak. In this case, the inward migration timescale is given as $\tau_{\text{migr,p}}$. The relation between $\tau_{\text{migr,p}}$ and the factor C is shown in the left panel of Figure 7. It can be seen that $\tau_{\text{migr,p}}$ is inversely proportional to C . This dependence comes from $\Sigma(r)$ in Equation (2). The exponent β is not changed by the multiplication of a constant factor (Equation (3)). If $\tau_{\text{migr,p}}$ is larger than 5×10^8 years (inner peak) or 6×10^8 years (outer peak), only inward migration is possible around the peak.

Protoplanets with various masses are formed both at the inner and outer convergence zones. We divide the region between 3 and 6.5 au into two areas. One is the area between 3 and 4.4 au, including the inner convergence zone (3.6 au). The other one is between 4.4 and 6.5 au, including the outer convergence zone (5.6 au). Objects inside the area between 3 and 4.4 au migrate to the inner convergence zone (Figure 1). Likewise, objects inside the area between 4.4 and 6.5 au migrate to the outer convergence zone. We checked the largest masses formed in these two areas at the end of a simulation.

The largest masses of protoplanets at the outer and inner areas substantially vary among simulation runs. The averages of the largest protoplanet masses at the inner and outer areas at the end of a simulation are shown in the right panel of Figure 7.

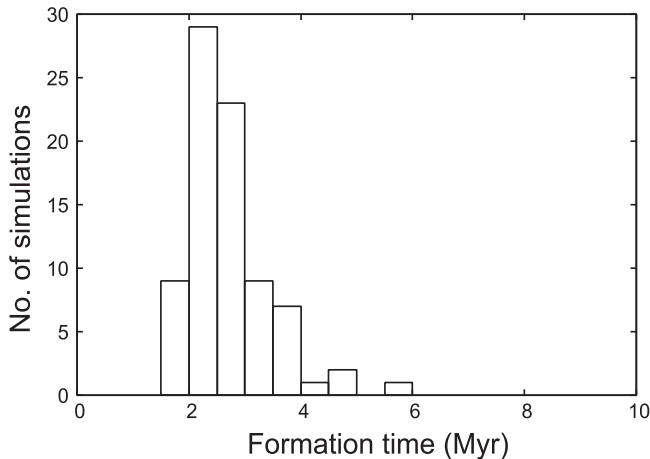


Figure 4. Distribution of the formation times of $10 M_{\oplus}$ objects. The width of each bin is 0.5 Myr. The mass of the largest object exceeds $10 M_{\oplus}$ in 81 runs.

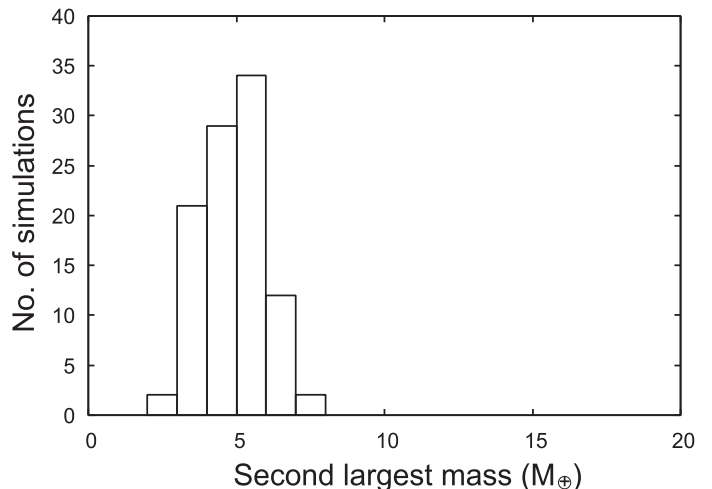
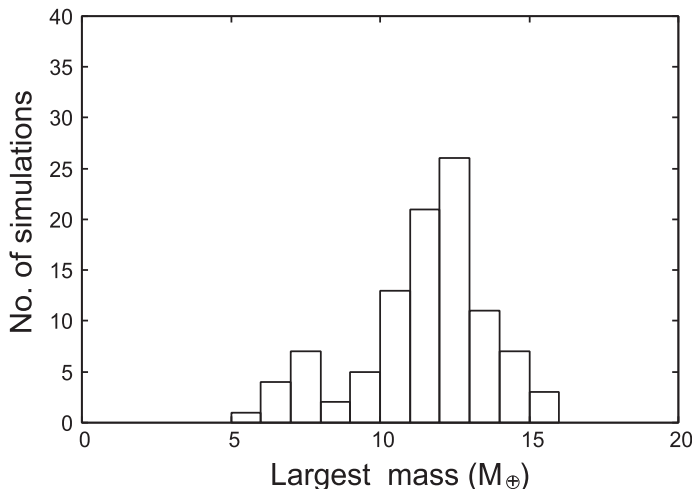


Figure 5. Distribution of the masses of the largest object (left) and the 2nd largest object (right). The width of a bin is $1 M_{\oplus}$.

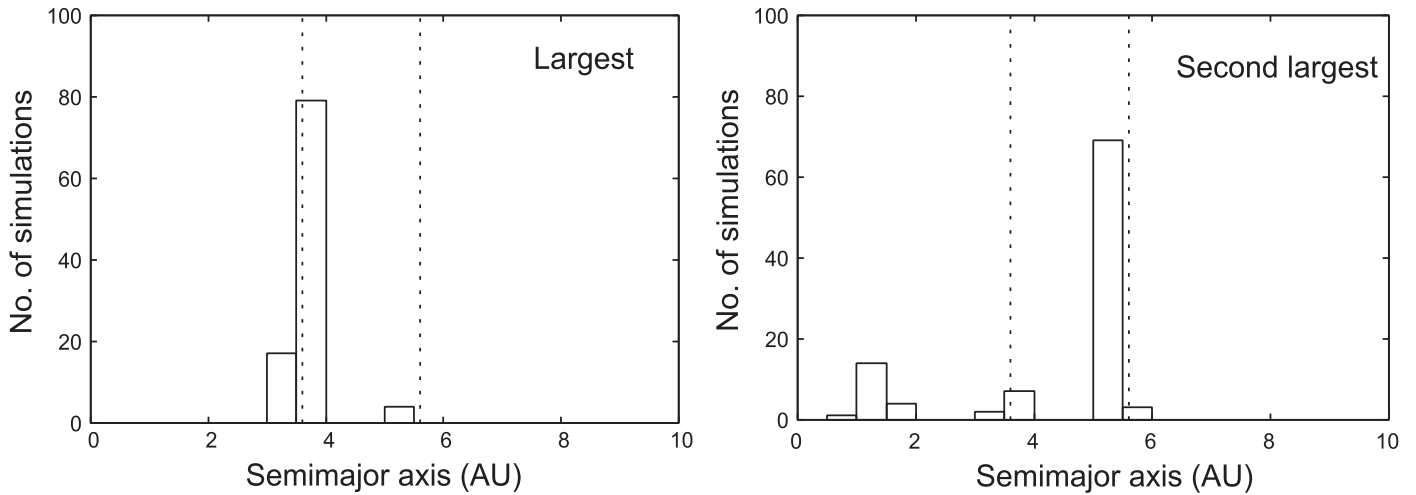


Figure 6. Distribution of the semimajor axes of the largest object (left) and the second largest object (right). The width of a bin is 0.5 au. The two vertical dotted lines are the inner and outer convergence zones.

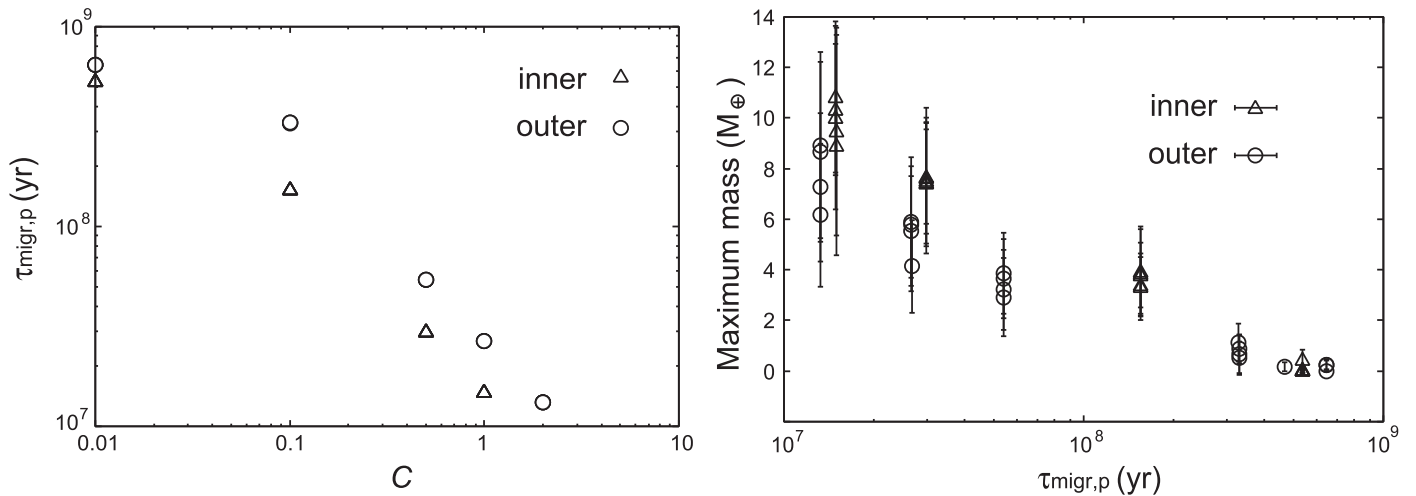


Figure 7. Relation between the factor C and $\tau_{\text{migr,p}}$ (left), and the relation between $\tau_{\text{migr,p}}$ and the average largest mass at the two convergence zones (right). Triangles are for the inner convergence zone and circles are for the outer convergence zone.

Error bars are standard deviations of 100 runs. It can be seen that the average largest mass depends logarithmically on $\tau_{\text{migr,p}}$. The largest mass in the inner area is slightly larger than that in the outer area, irrespective of $\tau_{\text{migr,p}}$. Therefore the largest object is formed at the inner edge of the dead zone.

It should be noted that the largest mass in the inner area is not affected by C at the outer peak and vice versa. In the right panel of Figure 7, it can be seen that the vertical scatter of data points is small. For example, at $\tau_{\text{migr,p}} = 5.5 \times 10^7$ years ($C = 0.5$) there are four data points for the largest mass at the outer area. The four points correspond to four different C at the inner area. The average mass varies only between 3 and 4 M_{\oplus} . This result suggests that a core can be formed even if there is only one convergence zone in a protoplanetary nebula.

From the right panel of Figure 7, the minimum height of a peak required for the formation of a core of a gas giant planet can be estimated. If the minimum core mass required for a gas giant is $10 M_{\oplus}$, the conditions are $C = 0.5$ for the inner peak and $C = 2$ for the outer peak, taking into account the standard deviation. The corresponding height of a peak should be larger than $\sim 10^3 \text{ g cm}^{-3}$.

The timescale to reach $10 M_{\oplus}$ depends on C at the inner peak. The timescale is 3.6 Myr for $C = 0.5$ and 2.6 Myr for

$C = 1$. Large C is preferable for core formation within a lifetime of a protoplanetary nebula.

3.3. Evolution of Surface Density

The effect of the evolution of gas surface density is studied using a 1D model given by Equation (6). Thirteen parameter sets are simulated (viscosity parameter, locations of inner and outer edges, and thickness of edges) as shown in Table 1. In addition, a case in which embryos are formed at $r_1 = 1$ au ($r_2 = 5.6$ au, $\Delta/h = 1$, $\alpha_0 = 10^{-2}$) is carried out. We performed 50 simulation runs for each set of parameters. Typical evolutions of the semimajor axes and masses of the top 10 objects in a model with $\alpha_0 = 10^{-3}$, $r_1 = 1$ au, $r_2 = 5.6$ au, $\Delta/h = 1$ are shown in Figure 8. As in previous models, the embryos are formed at the outer edge. At the beginning, the embryos collide with each other and grow to be $\simeq 2.0 M_{\oplus}$ objects in ~ 1 Myr around the outer edge. Because the convergence zone at the outer edge disappears in 1 Myr for this $\alpha_0 = 10^{-3}$, the objects of $\simeq 2.0 M_{\oplus}$ migrate to the inner edge, where a convergence zone remains. A $2.0 M_{\oplus}$ object grows further through collisions with other such objects. In the case shown in Figure 8, the largest mass exceeds $10 M_{\oplus}$.

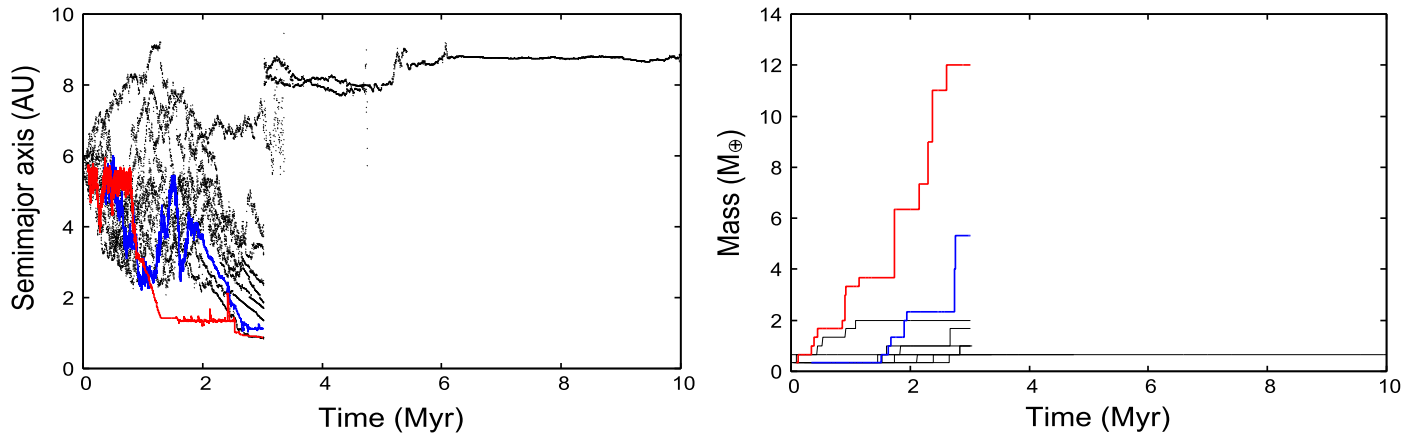


Figure 8. Evolution of the top 10 massive objects' semimajor axes (left) and masses (right) in a model with $\alpha_0 = 10^{-3}$, $r_1 = 1.0$ au, and $r_2 = 5.6$ au. The largest and second largest objects are shown by red and blue curves, respectively. The black curves correspond to the remaining eight objects.

Table 1
Parameter Sets Used in Simulations

α_0	r_1	r_2	Δ/h	N_{sur}
10^{-2}	1	5.6	1	38
10^{-3}	1	5.6	1	9
10^{-4}	1	5.6	1	22
10^{-5}	1	5.6	1	15
10^{-3}	0.1	5.6	1	22
10^{-4}	0.1	5.6	1	30
10^{-3}	0.1	12	1	43
10^{-4}	0.1	12	1	44
10^{-3}	3.6	5.6	1	38
10^{-2}	1	5.6	10	48
10^{-3}	1	5.6	10	41
10^{-4}	1	5.6	10	37
10^{-5}	1	5.6	10	39

Note. Viscosity parameter (α_0), positions of inner (r_1) and outer (r_2) edges, and the ratio between the thicknesses of the edges to the gas scale height (Δ/h). r_1 and r_2 are given in au. N_{sur} is the number of runs where the largest object remains at the end of the simulation among 50 simulation runs.

In Figure 8, the largest object grows through collisions of $\sim 2 M_{\oplus}$ objects. This evolution mode is different from that in the standard case in Section 3.1, where the largest mass evolves mainly through collisions with embryos of $1/3 M_{\oplus}$ (see Figure 3). For the parameter set of $\alpha_0 = 10^{-3}$, $r_1 = 1$ au, $r_2 = 5.6$ au, and $\Delta/h = 1$, the average largest mass is $15 M_{\oplus}$. The added mass due to collisions with objects larger than $4/3 M_{\oplus}$ is $10 M_{\oplus}$. Collisions with $1/3 M_{\oplus}$ occupy $2.7 M_{\oplus}$. On the other hand, in the standard case presented in Section 3.1, the average largest mass is $11 M_{\oplus}$. Collisions with $1/3 M_{\oplus}$ objects contribute $5.4 M_{\oplus}$. In the standard case, about half of the largest object were composed of $1/3 M_{\oplus}$ embryos.

If we use $r_1 = 3.6$ au instead of $r_1 = 1$ au, the average largest mass is $7.5 M_{\oplus}$. Collisions with $1/3 M_{\oplus}$ contribute $3.7 M_{\oplus}$. In this case, about half of the mass of the largest object was composed of $1/3 M_{\oplus}$ embryos. These results suggest that the distance between two edges is an important parameter. If this distance is short, the mass transport from the outer to the inner convergence zone is mainly composed of $1/3 M_{\oplus}$ mass embryos. If this distance is large, the mass transport is due to the migration of $2 M_{\oplus}$ objects.

If the location of the outer edge is $r_2 = 12$ au, the largest mass is much smaller than the typical core mass (Figure 9).

This is because the collision frequency at $r_2 = 12$ au is too small to grow to $2 M_{\oplus}$ and the migration timescale to the inner edge is long. The largest mass is $2.3 M_{\oplus}$ in Figure 9, much smaller than the threshold mass required for gas accretion.

In Figure 8, massive objects are ejected beyond 100 au at 3 Myr. This is due to a mutual scattering of large objects. If this happens, a core of $10 M_{\oplus}$ cannot be formed. However, the accretion of gas to form a Jovian planet is not included in this study. The accretion increases the mass of the envelope in ~ 0.3 Myr (Ikoma et al. 2000). This accretion should substantially change the orbital evolution of objects. Collision with the central star is another cause of mass loss. In the following, the largest mass means the largest mass attained in a simulation irrespective of a mass loss event, assuming that the largest object remains on the same orbit. Table 1 shows the number of runs in which the largest object survives at the end of a simulation. All of the largest objects survive in the simulations in the two previous sections. These results suggest that the distribution of gas torque significantly affects the orbital evolution of massive objects.

The left panel of Figure 10 shows the viscosity parameter dependence of the mass of the largest object. It can be seen that the largest mass has a peak at $\alpha_0 = 10^{-3}$. This trend can be explained by the right panel of Figure 10. This panel shows the time evolution of total mass inside 1.5 au. If α_0 is the largest (10^{-2}), the total mass inside 1.5 au quickly increases at 1 Myr. This is because the outer convergence zone disappears before 1 Myr. However, a substantial fraction of the objects at the inner edge are ejected or collide with the central star, and the total mass becomes less than that for $\alpha_0 = 10^{-3}$. It should be noted that $\alpha_0 = 10^{-2}$ cases (squares and diamonds) where embryos are formed at the outer edge are unphysical because the outer convergence zone disappears before the formation of embryos is completed.

For $\alpha_0 = 10^{-3}$, the formation timescale of $2 M_{\oplus}$ objects and the duration of the outer convergence zone are comparable. As α_0 decreases, the total mass decreases because the trapped mass at the outer convergence zone increases. In the case of $\alpha_0 = 10^{-5}$, the outer convergence zone lasts for 100 Myr. Some expelled objects from the outer convergence zone can infall to the inner convergence zone. However, the infalled objects quickly collide with the central star after they are expelled from the inner convergence zone. This is because the time evolution of the gas surface density is slow. The peak at the inner convergence zone is still steep, and the migration

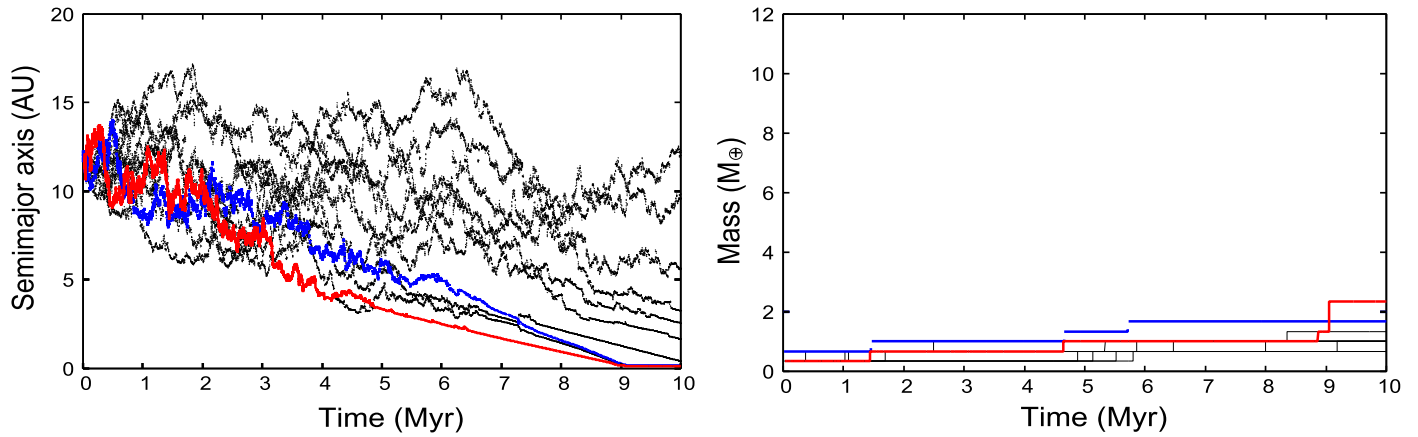


Figure 9. Evolution of the top 10 massive objects' semimajor axes (left) and masses (right) in a model with $\alpha_0 = 10^{-3}$, $r_1 = 0.1$ au, and $r_2 = 12$ au. The largest and second largest objects are shown by red and blue curves, respectively. The black curves correspond to the remaining eight objects.

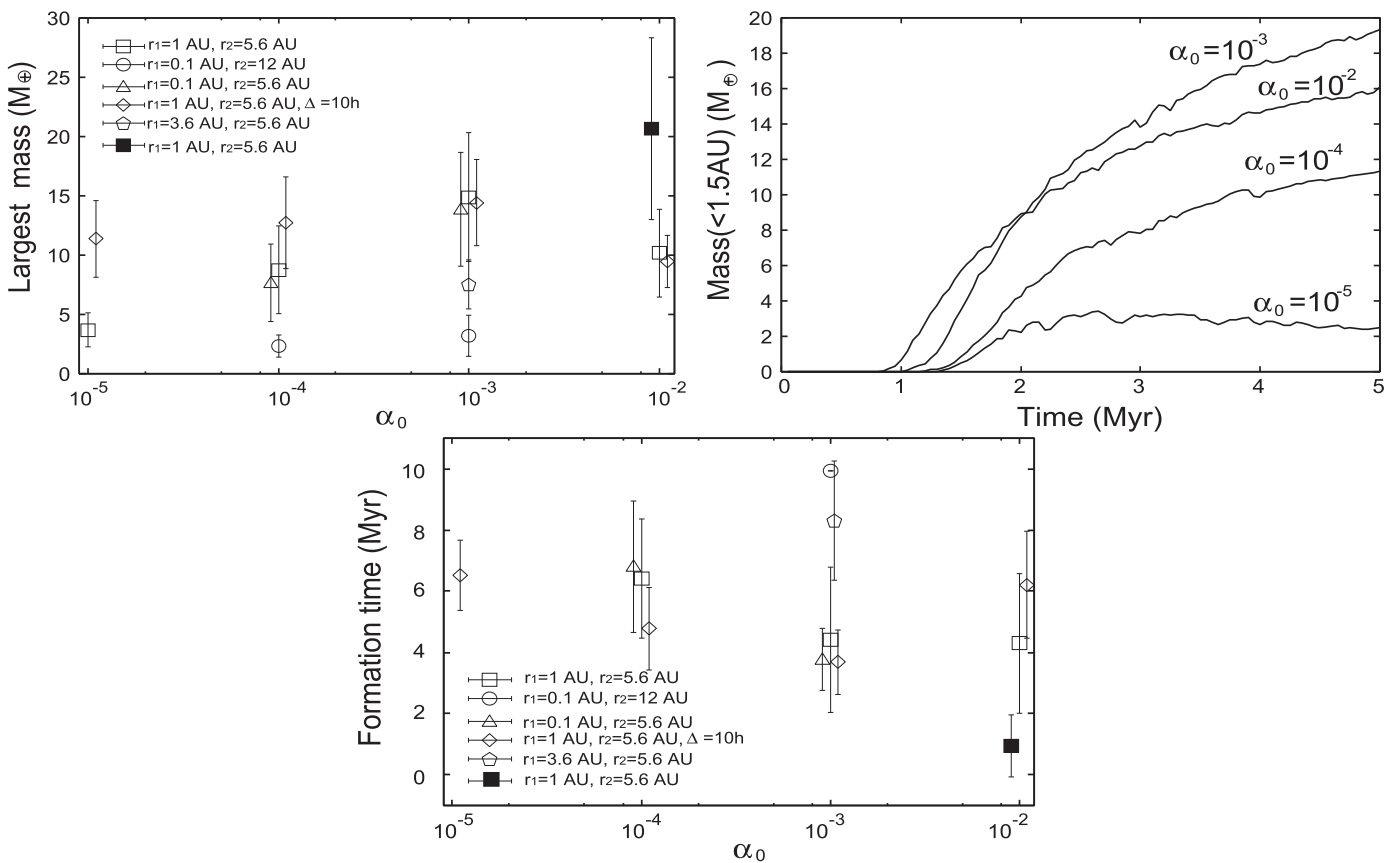


Figure 10. Viscosity parameter dependence of the mass of the largest object (left), time evolution of total mass inside 1.5 au (right), and formation time of $10 M_{\oplus}$ objects (bottom). In the left and bottom panels, $r_1 = 1$ and $r_2 = 5.6$ au (squares), $r_1 = 0.1$ and $r_2 = 12$ au (circles), $r_1 = 0.1$ and $r_2 = 5.6$ au (triangles), $r_1 = 1$ and $r_2 = 5.6$ au with $\Delta/h = 10$ (diamonds), $r_1 = 3.6$ and $r_2 = 5.6$ au (pentagons), and $r_1 = 1$ and $r_2 = 5.6$ au, with embryo formation at r_1 (filled square). Error bars show standard deviations of 50 runs. Data points are slightly shifted along the x -axis to avoid overlapping.

timescale is short (~ 0.1 Myr). This effect further decreases the total mass for $\alpha_0 = 10^{-5}$ other than scattering.

The bottom panel of Figure 10 compares the formation time of $10 M_{\oplus}$ objects. It can be seen that the formation time is the shortest at $\alpha_0 = 10^{-3}$. This trend can be clarified using the left panel of Figure 10, where the largest mass has a peak at $\alpha_0 = 10^{-3}$. The average formation time at $\alpha_0 = 10^{-3}$ is $\simeq 4$ Myr.

For $\alpha_0 = 10^{-2}$, most of the embryos should be formed at the inner edge because the outer convergence zone disappears

quickly (0.1 Myr). If the embryos are formed at the inner edge instead of the outer edge, the maximum mass is much larger, and the formation time is much shorter than that for other cases. In this case, the evolution is similar to that in Sándor et al. (2011); a newly placed embryo quickly collides with the largest object. This can be seen by the fact that the formation time of $10 M_{\oplus}$ object is ~ 0.5 Myr (a filled square in Figure 10), which is comparable to the duration of the embryo formation. Therefore, the results obtained for this case strongly depend on the formation scenario of the embryos. If the formation time

of embryos is much longer than 0.5 Myr, the formation time of a $10 M_{\oplus}$ object should be longer than 0.5 Myr.

The largest masses for the $\Delta/h = 10$ case are larger than those for $\Delta/h = 1$ cases. This is in contrast to the results of 2D simulations (Regály et al. 2013), where a $10 M_{\oplus}$ object is trapped only if $\Delta/h \leq 1.5$. In our simulations, a $10 M_{\oplus}$ object is formed inside the edge by collecting a $2 M_{\oplus}$ object. The trapping of infalling $10 M_{\oplus}$ objects and the formation of $10 M_{\oplus}$ objects might have a different Δ dependence. Wide edges correspond to wide convergence zones, which helps to capture objects, provided that a core candidate is inside the edge.

It should be noted that $\tau_{\text{migr,p}}$ at the inner edge is less than 1 Myr in this simulation. Therefore, the criterion obtained in the previous section is always satisfied. Mass transport from the outer edge is more important than in the previous two simulations (standard case and peak height variation). It can be seen that the viscosity parameter α_0 plays a critical role in the core formation. This parameter corresponds to the viscous evolution timescale of gaseous nebulae. If α_0 is too small, mass transport to the inner convergence zone is slow and the largest mass is small. Moreover, the inward migration is fast, leading to collisions with the central star because of a steep gradient of surface density distribution. Core formation preferentially proceeds at relatively large α_0 .

4. DISCUSSION

In Section 3.1, we showed that the largest mass is located at the inner convergence zone, although planetary embryos are formed at the outer convergence zone. The key to understanding this result is the distribution of torque applied to the objects shown in Figure 1. The height of the positive peak of Γ/Γ_0 at 3.2 au is roughly twice as that at 5.2 au. Moreover, the height of the peak of Σ at 3.5 au is also twice that at 5.5 au. Combining these two differences, the damping timescales for eccentricity and inclination at the inner convergence zones are shorter than those at the outer convergence zone by a factor of four (see Equations (2) and (5)). An embryo scattered to the inner convergence zone from the outer zone is trapped at the inner zone through the fast damping of eccentricity and inclination, followed by a collision with the massive object placed there.

The formation timescale of $10 M_{\oplus}$ mass objects is substantially longer than that obtained in Sándor et al. (2011). This is due to the long timescale of eccentricity and inclination damping in this study. In Sándor et al. (2011), the formation timescale of 0.4 Myr is strongly affected by the formation duration of embryos. This is because a $10 M_{\oplus}$ object can be formed only after the total mass of the system substantially exceeds $10 M_{\oplus}$. In Sándor et al. (2011) the total mass of the system is $27 M_{\oplus}$ at 0.4 Myr. The largest object efficiently captures the newly placed embryo at the outer edge. On the other hand, the formation timescale of ~ 2.5 Myr in this study is much longer than the duration of the embryo formation (0.5 Myr). Therefore, the formation timescale in this study reflects the dynamical properties of the system in this study.

From the simulations with modified heights of the peaks, it has been found that the height of a peak should be larger than $\sim 10^3 \text{ g cm}^{-3}$, or the migration timescale should be smaller than 10 Myr. Moreover, the 1D surface density evolution model revealed that the lifetime of the outer convergence zone is crucial for core formation. The average maximum mass takes a maximum at $\alpha_0 = 10^{-3}$ if the embryo formation proceeds at

the outer edge. If the embryos are formed at the inner edge when $\alpha_0 = 10^{-2}$, the maximum mass is large and formation time is short. Anyway, these results suggest that the viscosity parameter α_0 should be larger than 10^{-3} for core formation in this dead zone scenario. Moreover, the location of the outer edge of a dead zone is another important constraint. If $r_2 = 12$ au, a core cannot be formed because of slow orbital evolution. Based on recent numerical simulations (Dzyurkevich et al. 2013), the location of the outer edge varies between 5 and 20 au depending on input parameters. Therefore, the parameter $r_2 = 5.6$ au used in this study is a possible location of the outer edge.

If $\alpha_0 \geq 10^{-3}$ and $r_2 = 5.6$ au, the typical formation time of $10 M_{\oplus}$ objects is 3–4 Myr. On the other hand, the lifetime of gaseous nebulae ranges from 1 to 10 Myr (Haisch et al. 2001) and the typical lifetime is 2–3 Myr (Williams & Cieza 2011). Therefore, a core of a Jovian planet can be formed within the lifetime of a protoplanetary nebula. The formed core grows to a Jovian planet through the accretion of gas. The resultant planet may migrate outward by the same mechanism invoked in the Grand-tack scenario (Walsh et al. 2011).

5. CONCLUSION

We conducted N -body simulations to investigate the formation of cores of gas giants based on the basis of the scenario of Sándor et al. (2011). In this scenario, there are two convergence zones where the torque of the gas nebula is zero (3.6 and 5.6 au), which corresponds to the edges of the dead zone. Planetary embryos are continuously formed at the outer convergence zone. The correction of the damping timescales of eccentricity and inclination substantially changes the results obtained in Sándor et al. (2011). Excited motions of perturbed objects have a long duration. As a result, efficient mass transport from the outer to the inner convergence zone leads to the formation of the largest object at the inner convergence zone. On the other hand, objects of $\sim 6 M_{\oplus}$ are formed at the outer convergence zone. The formation timescale of an object of mass $10 M_{\oplus}$ is ~ 2.5 Myr, compared to 0.4 Myr, which obtained by Sándor et al. (2011). The formation of gas giants through gas accretion is still possible because the timescale is comparable to that of the nebula gas. We performed simulations in which we varied the heights of the peaks of the surface density distribution. The average largest mass depends logarithmically on the migration timescale around the peak. When the gas surface density distribution evolves by viscous accretion, the outer peak disappears on a short timescale and the evolution of the system is different from the fixed cases. The largest mass is formed at the inner convergence zone through the collisions between moderate masses of $\simeq 2.0 M_{\oplus}$ and the evolution is more stochastic than the fixed cases. In any case, the location of the largest mass is the inner convergence zone, corresponding to the inner edge of the dead zone. The mass of the largest object exceeds $10 M_{\oplus}$ if $\alpha_0 \geq 10^{-3}$ and $r_2 = 5.6$ au. If these conditions are satisfied, the typical formation time of $10 M_{\oplus}$ objects is 3–4 Myr. A core of a Jovian planet can be formed within the lifetime of a gas nebula in this scenario.

The authors thank Dr. Hirhoshi Kobayashi for stimulating discussions and Prof. Sei-ichiro Watanabe for his critical comments. The authors deeply appreciate the critical comments from Dr. Stuart Weidenschilling. This work is supported by the JSPS Grant-in-Aid for Scientific Research (C) 25400447.

REFERENCES

- Armitage, P. 2010, *Astrophysics of Planet Formation* (Cambridge: Cambridge Univ. Press)
- Chambers, J. E. 1999, *MNRAS*, 304, 793
- Cresswell, P., & Nelson, R. P. 2008, *A&A*, 482, 677
- Dzyurkevich, N., Turner, N. J., Henning, T., & Kley, W. 2013, *ApJ*, 765, 114
- Gammie, C. F. 1996, *ApJ*, 457, 355
- Haisch, K. E., Jr., Lada, E. A., & Lada, C. J. 2001, *ApJL*, 553, L153
- Hasegawa, Y., & Pudritz, R. E. 2011, *MNRAS*, 417, 1236
- Hellary, P., & Nelson, R. P. 2012, *MNRAS*, 419, 2737
- Ikoma, M., Nakazawa, K., & Emori, H. 2000, *ApJ*, 537, 1013
- Kato, M. T., Fujimoto, M., & Ida, S. 2010, *ApJ*, 714, 1155
- Kretke, A., & Lin, D. N. C. 2007, *ApJL*, 664, L55
- Levison, H. F., Thommes, E., & Duncan, M. J. 2010, *ApJ*, 139, 1297
- Lyra, W., Johansen, A., Zsom, A., Klahr, H., & Piskunov, N. 2009, *A&A*, 497, 869
- Paardekooper, S.-J., & Mellema, G. 2006, *A&A*, 459, L17
- Regály, Z., Sándor, Z., Csomós, P., & Ataiee, S. 2013, *MNRAS*, 433, 2626
- Sándor, Z., Lyra, W., & Dullemond, C. P. 2011, *ApJL*, 728, L9
- Sirono, S. 2011, *ApJL*, 733, L41
- Tanaka, H., Takeuchi, T., & Ward, W. R. 2002, *ApJ*, 565, 1257
- Walsh, K. J., Morbidelli, A., Raymond, S. N., O'Brien, D. P., & Mandell, A. M. 2011, *Natur*, 475, 206
- Weidenschilling, S. J. 1977, *MNRAS*, 180, 57
- Williams, J. P., & Cieza, L. A. 2011, *ARA&A*, 49, 67